

# Electro-optically tunable Brillouin microlasers on lithium niobate platform

Chuntao Li,<sup>1,4,#</sup> Jiale Deng,<sup>2,#</sup> Xingzhao Huang,<sup>2,#</sup> Xiaochao Luo,<sup>3,5</sup> Renhong Gao,<sup>4</sup> Jintian Lin,<sup>3,5,\*</sup> Huakang Yu,<sup>2,\*</sup> Jianglin Guan,<sup>1,4</sup> Jacob B. Khurgin,<sup>6</sup> Zhiyuan Li,<sup>2</sup> Ya Cheng<sup>1,3,4,7,8,9,10,\*</sup>

<sup>1</sup>State Key Laboratory of Precision Spectroscopy, East China Normal University, Shanghai 200062, China

<sup>2</sup>School of Physics and Optoelectronics, State Key Laboratory of Luminescent Materials and Devices, South China University of Technology, Guangzhou 510460, China

<sup>3</sup>State Key Laboratory of High Field Laser Physics, Shanghai Institute of Optics and Fine Mechanics, Chinese Academy of Sciences, Shanghai 201800, China

<sup>4</sup>The Extreme Optoelectromechanics Laboratory (XXL), School of Physics and Electronic Science, East China Normal University, Shanghai 200241, China

<sup>5</sup>University of Chinese Academy of Sciences, Beijing 100049, China.

<sup>6</sup>Department of Electrical and Computer Engineering, JohnsHopkins University, Baltimore, MD 21218, USA

<sup>7</sup>Shanghai Research Center for Quantum Sciences, Shanghai 201315, China

<sup>8</sup>Hefei National Laboratory, Hefei 230088, China

<sup>9</sup>Collaborative Innovation Center of Extreme Optics, Shanxi University, Taiyuan 030006, China

<sup>10</sup>Collaborative Innovation Center of Light Manipulations and Applications, Shandong Normal University, Jinan 250358, China

<sup>#</sup>Chuntao Li, Jiale Deng, and Xingchao Huang contributed equally to this work.

<sup>\*</sup>Corresponding authors: jintianlin@siom.ac.cn; hkyu@scut.edu.cn; ya.cheng@siom.ac.cn

Miniature, monolithic, tunable sources of coherent radiation with narrow linewidths and low noise are highly sought after for photonic integration. Brillouin lasers, known for their intrinsically narrow linewidths, present an appealing solution. However, achieving the strong optomechanical coupling necessary for lasing in optical microresonators remains challenging due to the difficulty of simultaneously confining optical and acoustic modes

with substantial modal overlap. Additionally, most Brillouin lasers lack tunability. Lithium niobate (LN) emerges as an excellent platform for integrated photonics, offering large photoelastic coefficients and electro-optic tunability. In this work, we demonstrate strong optomechanical interactions in a 117- $\mu\text{m}$ -diameter LN microdisk resonator, achieved through post-fabrication dispersion management and enhanced mode matching enabled by the large off-diagonal elements of the photoelastic tensor. This approach yields an impressive optomechanical coupling rate of up to 30 kHz per photon, resulting in a tunable, integrated Brillouin microlaser with an intrinsic linewidth of 118 Hz and a low lasing threshold of 3.15 mW — a remarkable performance for such a compact device. Furthermore, we demonstrate electro-optic tuning of the microlaser with an efficiency of 43.2 kHz/V, showcasing the versatility of LN for next-generation tunable photonic systems.

## **Introduction**

Narrow linewidth tunable laser sources provide spectral purity required for a wide range of applications ranging from coherent communications (1), next-generation data center networks, to quantum sensing (2,3), and miniaturized atomic clocks (4). In recent years, there is an ever-growing demand to translate such highly coherent light sources from laboratory benchtop to photonic integrated devices due to their low threshold, compact size, high robustness, lower cost and power consumption, enabling systems-on-chip solutions for the aforementioned applications (5-10). One promising approach to generate narrow-linewidth tunable microlaser is leveraging optical gain from stimulated Brillouin scattering (SBS) overcoming round-trip loss in an optical microcavity, to narrow the pump laser linewidth by many orders of magnitude (5-7). The conventional approach for realizing integrated Brillouin lasers (BLs) involves utilizing whispering gallery mode (WGM) microlaser cavities for simultaneous confinement of optical and acoustic modes and stringent fulfillment of both energy and momentum conservation conditions, so as to enhance Brillouin optomechanical coupling.

To this end, the periphery of the Brillouin lasing resonator is frequently suspended in air to prevent either optical or acoustic coupling of the optical and mechanical modes to the substrates, so as to ensure simultaneous confinement of optical and acoustic modes. To obtain a maximum Brillouin gain, the phase-matching conditions are predominantly rendered for effective optomechanical energy transfer, while efficient spatial overlapping between the optical and mechanical modes is of primary importance through the underlying

physical effects, i.e., moving boundary and photoelastic effects. Meanwhile, the Brillouin self-cancellation effect needs to be avoided for enhancing the optomechanical coupling (11).

Generally, since the mechanical wave frequency is orders of magnitude lower than the optical frequency, such narrow-linewidth Brillouin microlasers have been successfully demonstrated either in millimeter-to-centimeter-scale resonators with one or multi free spectral ranges to match the Brillouin frequency shift (5,6,12), or in heavily multimode microresonators where the frequency difference of the distinct transverse optical modes accidentally matches the frequency shift (13-16). However, both these approaches come at the cost of reduced optomechanical coupling which in turn requires much higher pump power levels, caused either by large modal volume, or limited modal overlaps. Moreover, real-time tuning of the Brillouin microlasers which is crucial for photonic applications, has yet to be demonstrated.

It is worth noting that Brillouin microlasers integrated on Si, SiN and SiO<sub>2</sub> platforms have been demonstrated (5-7,14-18), but none of these materials simultaneously have good photoelastic, electro-optical, or nonlinear optical properties combined with low loss that are essential for development of versatile photonic integrated circuits (PICs). Lithium niobate on insulator (LNOI) does possess all these properties and more (19-22), which are crucial for ensuring that such BLs outperform all other on-chip counterparts in strong optomechanical coupling and electro-optically tunable PICs. However, achieving Brillouin microlaser in LNOI has proven to be a daunting task due to difficulty of simultaneous confinement of optical and acoustic modes, significant acoustic mode leakage to the SiO<sub>2</sub> substrate, and ensuring strong coupling between them by maximizing the utilization of the photoelastic tensor as large as possible.

In this work, we overcome these challenges and demonstrate strong optomechanical coupling with two sets of fundamental cavity modes with orthogonal polarizations in an LNOI microresonator by dispersion engineering. Effective post-fabrication dispersion management was performed by introducing weak perturbation in the suspended microdisk via a coupling tapered fiber waveguide for agile tuning the modal interval of the modes to match the Brillouin frequency, which significantly relaxes the phase-matched modes selection requirement, so as to simultaneously ensure strong coupling between light and acoustic modes through the utilization of large photoelastic tensor of lithium niobate crystal. Consequently, an optomechanical coupling rate per photon up to 32 kHz was realized,

approaching a three-fold improvement compared to the state of the art (17). Brillouin lasing was observed with 118-Hz intrinsic linewidth and 3.15-mW threshold power. Furthermore, enabled by dispersion management, tuning of the integrated BL was observed over a spectral range exceeding 9 nm. Electro-optic tuning of the integrated BL demonstrated here for the first time shows great potential in large-scale photonic integration with tunable features, and paves the way for development of compact PICs with applications ranging from coherent information processing to precision metrology.

## Results

### I- Enabling Brillouin lasing in a small diameter LNOI microresonator

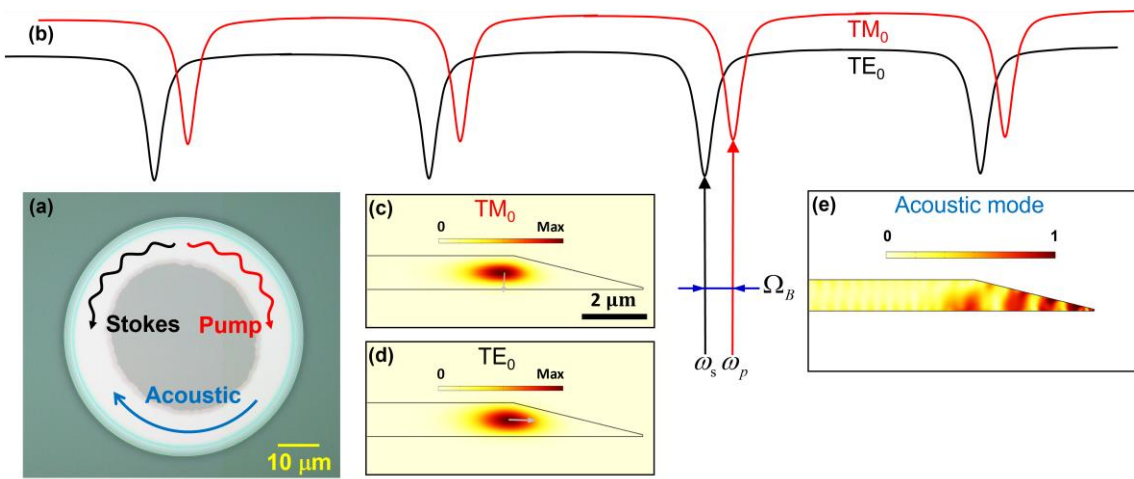


**Fig. 1 Schematic diagram of the stimulated Brillouin lasing.** (a) Sketch of the waves in backward Stokes Brillouin laser (SBL) in an LNOI microresonator. (b) Schematic transmission spectra for the two sets of fundamental cavity modes with orthogonal polarizations, i.e.,  $TM_0$  (red line) and  $TE_0$  (black line). Inter-modal stimulated Brillouin scattering occurs while the dual-resonance condition is satisfied for the pump ( $\omega_p$ ) and Stokes ( $\omega_s$ ). The modal profiles of (c)  $TM_0$  and (d)  $TE_0$  optical modes, and (e) hybridized WGM-like and dilatational shear acoustic modes whose overlap is responsible for strong optomechanical coupling.

To maximize Brillouin gain, we designed and fabricated mesoscopic suspended microdisks to achieve the dual-resonance condition, essential for matching the small Brillouin gain shift (Fig. 1). For LNOI microdisks with a diameter of  $100\ \mu\text{m}$  and subwavelength thickness, the shear-mode Brillouin shift was approximately 10 GHz. To satisfy the phase-matching condition, we utilized two sets of fundamental cavity modes with orthogonal polarizations:  $TM_0$  and  $TE_0$ . This choice was motivated by the presence of significant off-diagonal photoelastic tensor elements ( $p_{55}$  and  $p_{56}$ , see Supplementary Materials), which facilitate strong optomechanical coupling between these orthogonally polarized modes with similar spatial distributions. Numerical simulations confirmed the existence of WGM-like optical

modes and dilatational shear acoustic modes within the 10 GHz frequency range (see Supplementary Materials). This close frequency matching enabled the simultaneous fulfillment of the phase-matching and dual-resonance conditions for SBS through pump wavelength tuning.

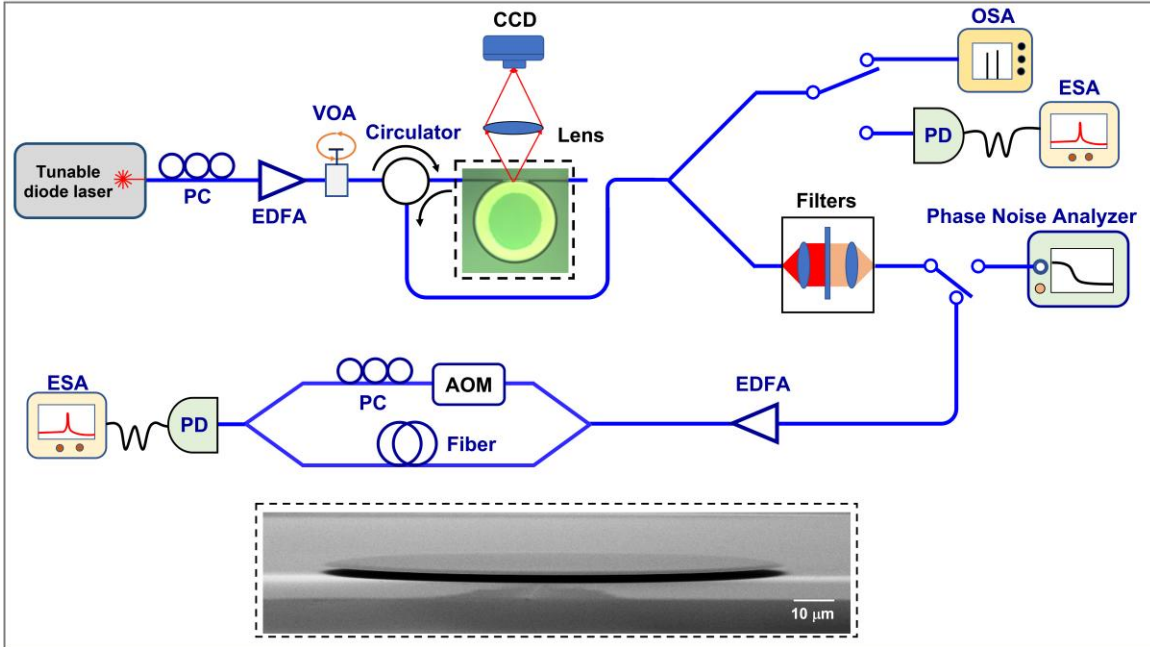


**Fig. 2 Experimental setup for characterization of the Brillouin microlaser.** Here, AOM denotes acousto-optic modulator that shifts the light frequency by 100 MHz is denoted, PC is polarization controller, EDFA is erbium-doped fiber amplifier, and VOA is variable optical attenuator. Inset: Scanning-electron-microscope (SEM) image of the suspended microresonator.

Experimentally, the suspended LNOI microdisk was fabricated by femtosecond laser photolithography assisted chemo-mechanical etching (9,23), with a diameter of 117  $\mu\text{m}$ , a thickness of 800 nm, and a wedge angle of the sidewall of 15° sitting on a smaller silicon dioxide pillar, as depicted in the Fig. 1(a). It is of particular concern that the periphery of the resonator is suspended in air, which readily provides tight confinements of both optical and acoustic modes (24-26) inside the microresonator. For the 117- $\mu\text{m}$ -diameter of LNOI microresonator, the free spectral ranges (FSRs) are around 390 GHz for the  $\text{TE}_0$  mode and 370 GHz for the  $\text{TM}_0$  mode. As the FSRs of the  $\text{TM}_0$  and  $\text{TE}_0$  modes differ by 5 %, dual-resonance condition of the pump of the  $\text{TM}_0$  mode and Stokes light of the  $\text{TE}_0$  mode become accessible every 60 nm over the wavelength tuning range (from 1510 nm to 1610 nm) (14). Moreover, post-fabrication dispersion management was performed by coupling the microdisk with a tapered fiber to introduce weak perturbation, so as to agilely tune the

frequency interval of the cavity modes to match the Brillouin frequency shift, enabling the efficient utilization of the large photoelastic tensor and wide tuning of the microlaser.

The experimental setup is schematically illustrated in Fig. 2 (see Materials and Methods for details). To realize the dual-resonance condition for matching the narrow Brillouin gain shift, a continuous-wave (CW) pump light at the wavelength of 1555.81 nm was injected into the LNOI microresonator. In order to facilitate the Brillouin laser around 1555 nm, fine dispersion trimming was achieved by elaborately coupling the microdisk with a tapered optical fiber to tune the resonant frequency interval of the two optical WGMs (see Section IV). While increasing the input power of pump light, a backward Stokes Brillouin laser (SBL) signal could be observed at the wavelength of 1555.89 nm recorded by an optical spectral analyzer (OSA), as shown in Fig. 3(a). From the spectrum, we found that the wavelength interval between the pump wavelength and the SBL signal was  $\sim 0.08$  nm, corresponding to Brillouin frequency shift  $\Omega_B$  of  $\sim 10$  GHz. This Brillouin shift  $\Omega_B$ , equal to the radio-frequency (RF) beat note signal of the pump light and the backward SBL, was further identified at a frequency centered at 10.3 GHz using a high-speed photodetector (PD) connected with a real-time electrical spectral analyzer (ESA), as shown in Fig. 3(b). The dependence of the backward SBL power on the on-chip pump power was also measured, as shown in Fig. 3(c). Above the pump threshold of 3.15 mW, the SBL power grows linearly with the increasing pump power, a telltale sign of stimulated emission. From linear fitting, the slope efficiency was determined as high as 6.8% with maximized output SBL power of  $\sim 0.4$  mW. According to the theory of SBL threshold as in the Supplementary Materials, for the over-coupled condition for pump light in the experiment, we may obtain Brillouin gain  $g_b = 9.97 \times 10^{-11}$  cm/W for pump light of  $\lambda = 1555.8$  nm and cavity circumference of  $L = \pi \cdot 117$   $\mu\text{m}$ . As the coupling plays an important role in determining the SBL threshold, even lower threshold could be possible if we further optimize the tapered fiber coupling (15,27).

Enabled by agile dispersion management through tapered fiber coupling, and in addition to the dual resonance with orthogonally polarized fundamental optical WGMs, a large number of spatially high-order optical WGMs also match the Brillouin shift. These high-order modes can be utilized to tune the microlaser, even within this small microresonator. When the pump wavelength was tuned from 1555.81 nm to shorter wavelength, e.g., 1553.89 nm,

1549.11 nm, 1546.30 nm, the Brillouin lasing signal was shifted from 1555.89 nm to 1546.39 nm, corresponding to a tunable spectral range of  $> 9$  nm, as shown in Fig. 3(d).

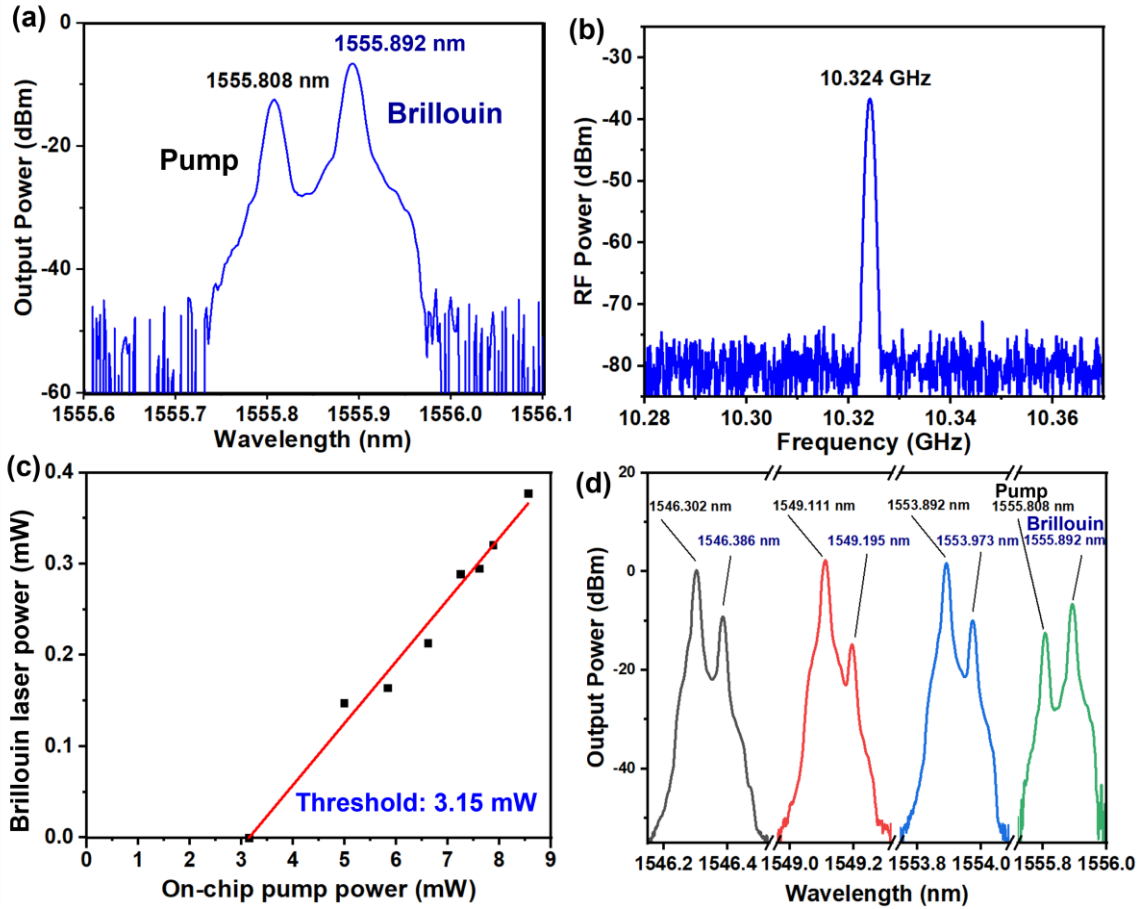


**Fig. 3 Tunable SBL lasing** (a) Optical spectrum of the backward SBL signal. (b) The radio-frequency (RF) beat note signal generated by mixing the pump light and the SBL. (c) Power of backward SBL as a function of the on-chip pump power. (d) Optical spectrum of the tuning of the SBL.

## II- Real-time electro-optic tuning of the Brillouin laser

The electro-optic tuning capability is one of the most appealing features for lithium niobate (LN). To perform real-time electro-optic (EO) tuning, two in-plane Cr microelectrodes perpendicular to X principal axis of LN were designed and monolithically integrated on the left and right sides of the microresonator, as shown in the inset of Fig. 4(b). The gap of the electrode pair was set as  $139 \mu\text{m}$ . This electrode pair would then produce electric field oriented to X principal axis, as shown in Fig. 4(c), and enable the utilization of EO coefficient  $r_{22}$ , leading to a dominant modification in the in-plane (X-Y plane) refractive index ellipsoid of the half microdisk [28]. Such configuration would ensure electro-optical tuning of effective refractive index of the Stokes optical mode (i.e.,  $\text{TE}_0$  mode) in the

microdisk, while not affecting the pump optical mode (i.e.,  $TM_0$  mode). Consequently, when the pump wavelength was fixed at 1555.808 nm (resonant with  $TM_0$  mode) upon applying a bias voltage, the generated SBL signal would be red-shifted correspondingly, as recorded by the RF beat note signal in Fig. 4(a). When the bias voltage was increased from 0 V to 200 V, the RF beat note signal shifted with 8.64 MHz. Figure 4(b) shows the dependence of this SBL frequency drift on the bias voltages with an EO tuning efficiency of the SBL of 43.2 kHz/V, which could be further enhanced by subsequent optimization of the electrode design.

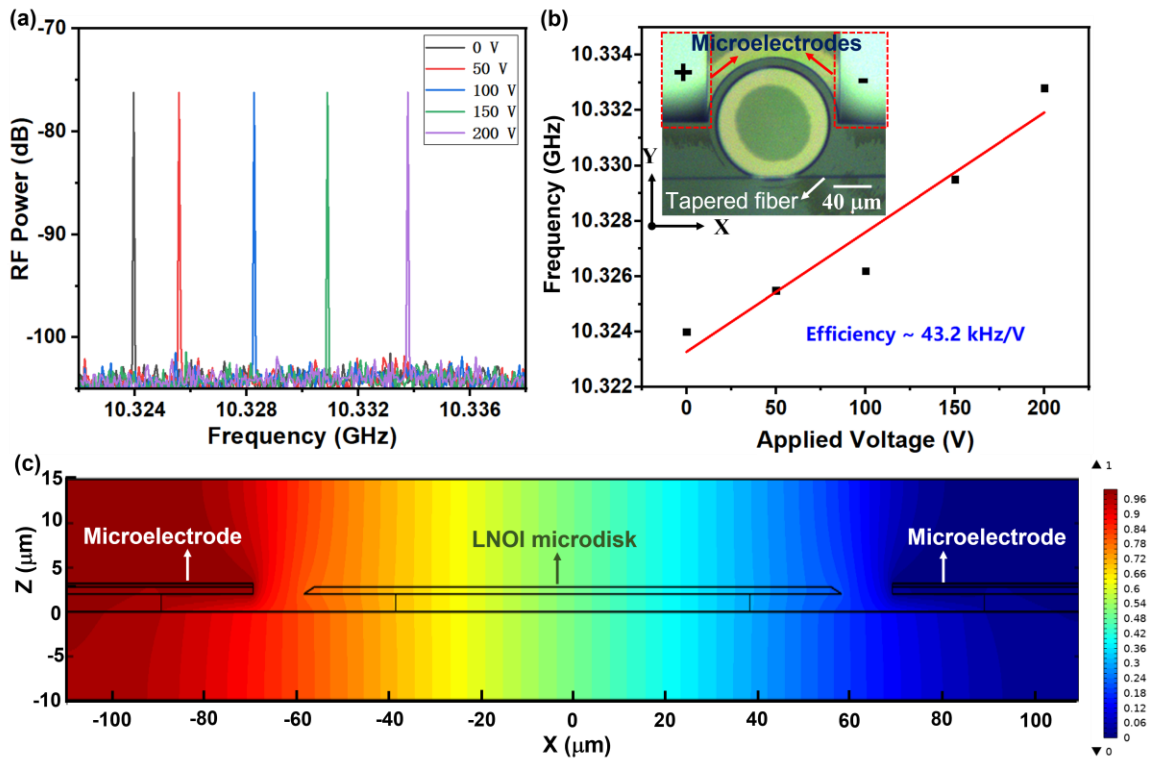


**Fig. 4 Electro-optic tuning of the SBL.** (a) RF beat note signal shifts with the varied bias voltage recorded with high resolution of 100 Hz. (b) RF beat note signal frequency drift as a function of the applied bias voltage. (c) Electric potential produced by the bias voltage applied on the microelectrodes.

### III- Measurement of the lasing linewidth

The linewidth of the SBL is one of the crucial features to be determined. The frequency noise of the backward SBL measured by the commercially available laser phase noise analyzer based on correlated self-heterodyne method and evaluated by  $\beta$ -separation line integration method (17) is shown in Fig. 5(a). The white-frequency-noise floors  $N_{wfn}$  of the backward SBL was measured to be  $37.4 \text{ Hz}^2/\text{Hz}$ , revealing short-term linewidth  $L_{st}$  of 117.5 Hz ( $L_{st} = N_{wfn} \times \pi$ ) (29). And the dependence of the short-term linewidth of the SBL on

the SBL power was also characterized, as the results plotted in Fig. 5(b). The linewidth almost linearly increases as the growth of the SBL power, confirming that the linewidth corresponds to intrinsic linewidth. Such ultra-narrow linewidth is resulted from the narrow Brillouin gain bandwidth and the short lifetime of the Brillouin phonon (5,7). For comparison with previous results obtained without accounting for the effects of optical coherence—arising from the length-limited delay in self-heterodyne narrow-linewidth signals, the phase noise and intrinsic linewidth of the SBL measured without using  $\beta$ -separation line integration method, as described in Ref. [18], are presented in Supplementary Materials. These measurements revealed an underestimated intrinsic linewidth of approximately 0.5 Hz.

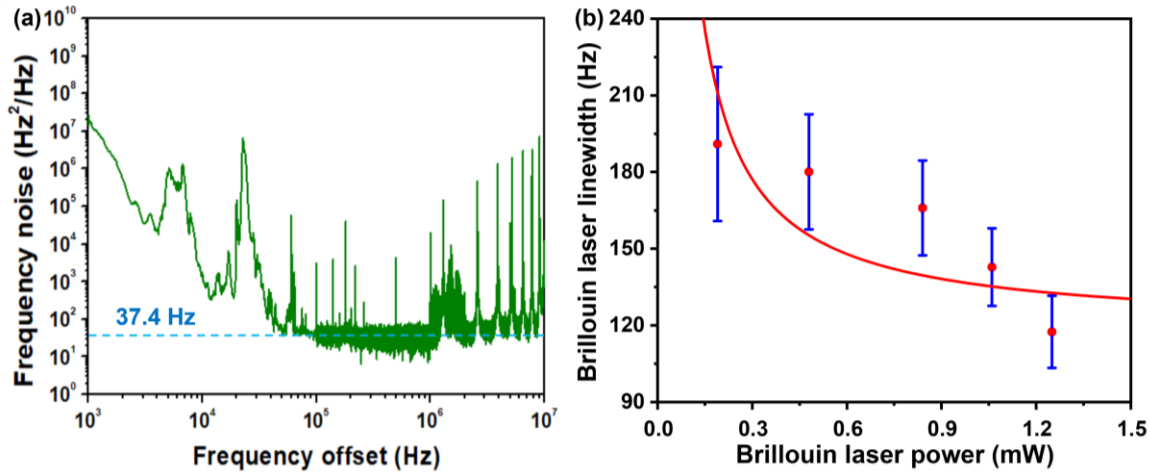


**Fig. 5 Measurement of the intrinsic linewidth of the SBL.** (a) The frequency noise spectrum of the backward SBL. (b) Intrinsic linewidth of the backward SBL as a function of the SBL power (blue lines) and the theoretical calculation of the SBL linewidth (red curve).

Theoretically, the linewidth of SBL can be given by (30),

$$\Delta\nu_{SBL} = \frac{\Gamma^2}{(\gamma + \Gamma)^2} \frac{\hbar\omega_s^3}{4\pi Q_T Q_{ex} P_{SBL}} n_{th} + \frac{\gamma^2}{(\gamma + \Gamma)^2} \Delta\nu_{pump} \quad (1)$$

where the first term represents the fundamental linewidth and second part represents the contributing factor of linewidth from the transferred pump noise. If the linewidth of pump laser is relatively large or satisfying the condition of mechanical lasing (31) (i.e.,  $\gamma_s \gg \Gamma_m$ ), the linewidth of SBL was mainly contributed by the pump noise. If stokes mode dissipation  $\gamma_s$  is far smaller than mechanical mode dissipation  $\Gamma_m$  ( $\gamma_s \ll \Gamma_m$ ), stokes field would experience linewidth-narrowing (14). We can calculate fundamental linewidth to be 53 Hz based on the result from our experiment (see Supplementary Materials for details), which

agrees well with the measured result. We can see the main contribution of linewidth was coming from the transferred pump laser noise, leading to much larger linewidth than the sub-hertz linewidth as in Ref. [5], which is reasonable since the Pound–Drever–Hall (PDH) technique was not applied here for stabilizing the frequency of the pump laser. Further improvement of the optical Q factor (e.g., one order of magnitude augment) of the sub-millimeter-diameter microcavity together with minimized transferred pump laser noise would enable narrower SBL laser linewidth even to sub-hertz level akin to the much large resonator counterparts (5,32).

#### IV- Post-fabrication dispersion engineering

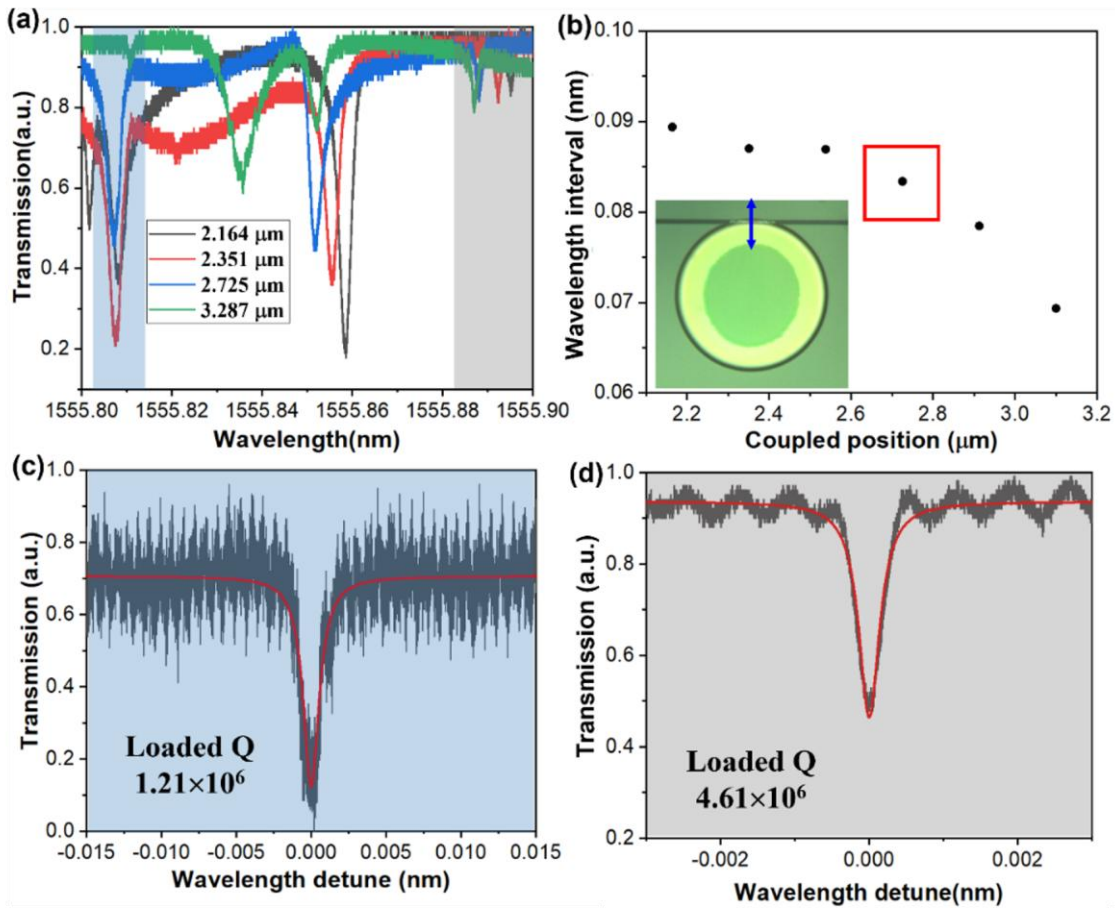


**Fig. 6 Dispersion management.** (a) Transmission spectra of the two modes varied with the coupled position, where the two modes are labeled with color rectangles. (b) Wavelength interval between the two modes as a function of the coupled position. Inset: Optical microscope image of the tapered fiber placed in contact with the top surface of the microdisk. (c) Loaded Q factor of the pump mode. (d) Loaded Q factor of the Brillouin Stokes mode.

Moreover, to facilitate Brillouin lasing around 1555.8 nm and ever-wider spectral range tuning, fine dispersion trimming could be achieved by elaborately coupling the microdisk

with a tapered optical fiber to tune the resonant frequency interval of the two optical WGMs. Here, weak perturbation was introduced into the two radial modes  $TM_0$  and  $TE_0$  to change the modal effective refractive indices and in turn trim the wavelength interval wavelength, via spatially selectively changing the coupled position between the tapered fiber and the microdisk (9). Here, the coupled position is defined as the distance from the periphery of the microdisk to the center of the tapered fiber. The resonant wavelengths of these two modes as functions of the coupled position were measured, as shown in Fig. 6(a). The fundamental  $TE_0$  mode undergoes blue shift when the tapered fiber was adjusted to the coupled position (from 2.16  $\mu\text{m}$  to 3.29  $\mu\text{m}$ ) more closed to the microdisk center, whilst the  $TM_0$  mode almost keeps fixed. As a result, the wavelength interval endures decrease during changing the coupled position, as shown in Fig. 6(b). When the coupled position was chosen as 2.725  $\mu\text{m}$ , the wavelength interval was measured to be 0.084 nm (i.e.,  $\sim 10.3$  GHz), exactly corresponding to the Brillouin frequency shift. And the mode structures of these two modes are shown in Figs. 6(c) and 6(d), exhibiting loaded Q factors of  $1.21 \times 10^6$  and  $4.61 \times 10^6$ , respectively. The ultra-high Q factor more than  $4 \times 10^6$  will enable ultra-narrow linewidth Brillouin lasing.

## V- Modeling of the Stokes Brillouin microlaser

To interpret the experimental observations, we derived both analytical and numerical models that describe the behavior of SBL oscillation inside the LNOI microresonator. It is known that both shear and longitudinal acoustic waves exist in such a microresonator with its periphery suspending in air. As the measured value of Brillouin shift around 10.3 GHz, one could readily identify that it was the shear acoustic wave that was involved in the SBS process. This is because velocity  $V_A$  of the shear acoustic wave in lithium niobate around 3600 m/s (24), corresponding to a calculated Brillouin shift  $\Omega_B = \frac{4\pi n V_A}{\lambda_p}$  to be  $2\pi \cdot 10.1$  GHz, a value close to the experimental results. We performed the numerical simulations showing that phase-matched SBS occurred between a  $TM_0$  (with azimuth mode number of  $m_p = 422$  @ 1555.808 nm) and  $TE_0$  ( $m_s = -455$  @ 1555.891 nm) with frequency discrepancy of 10.3 GHz, as shown in Fig. 7. Following the phase matching condition, ( $M = m_p - m_s$ ), we could identify a hybridized WGM-like and dilatational shear acoustic mode at 10.326 GHz ( $M = 877$ ), with its location closer to the edge of the resonator. Figures 7 (a) and (b) show the main components of the two interacting optical mode. The subscripts  $p$

and  $s$  represent the pump and SBL light, and  $r(z)$  represents the radial (height) component of the electric fields.

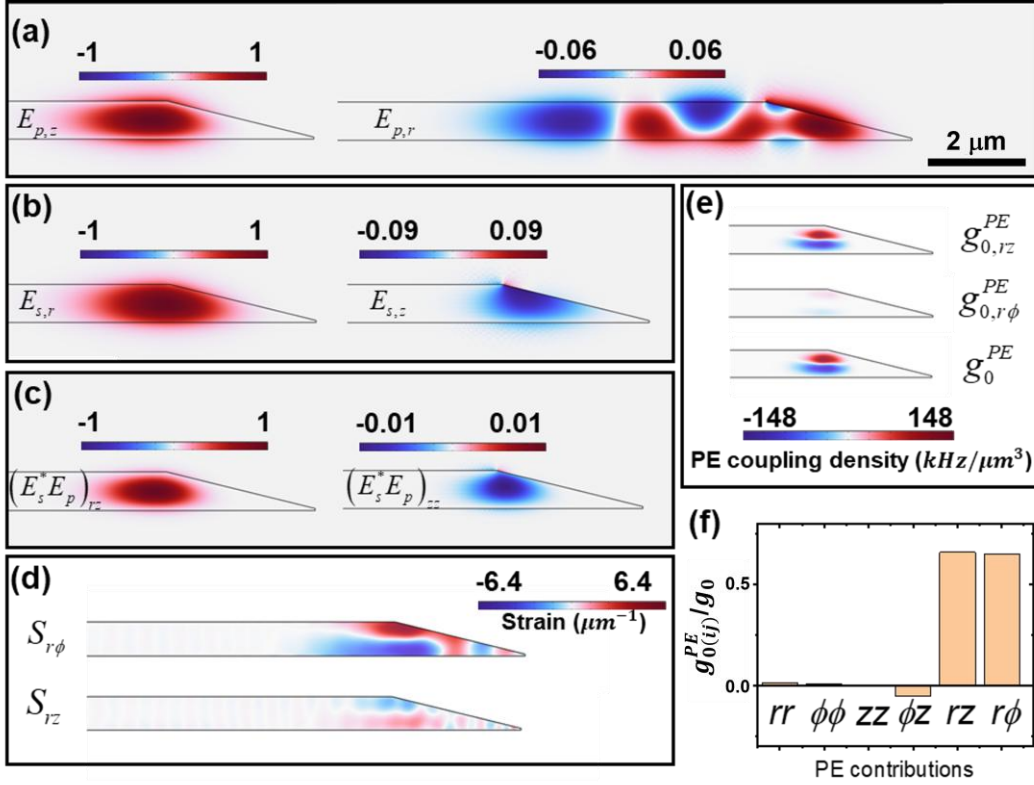


**Fig. 7 Efficient opto-mechanical coupling.** Optical mode electric field distribution of (a) the pump light (TM<sub>0</sub>-polarized,  $m = 422$  @ 1555.808 nm) and (b) the Brillouin laser modes (TE<sub>0</sub>-polarized,  $m = -455$  @ 1555.891 nm). (c) Overlap integral of the electric fields of the pump light and the Brillouin laser, showing only the two largest components, namely  $(E_s^* E_p)_{rz}$  and  $(E_s^* E_p)_{zz}$ . (d) Dominant normalized strain components for the phase-matched mechanical mode at 10.326 GHz. (e) Spatial distribution of the major photoelastic (PE) coupling terms identified in (f) and the net coupling. (f) Contribution of each coupling term to the PE overlap integral.

In order to get a more quantitative insight on how the two optical modes actually couple to the identified mechanical modes in the microresonator, individual components of the optomechanical coupling rate, including the photoelastic (PE) and moving boundary (MB) effects, were investigated (See Supplementary Materials for more details). It was found that the PE effects dominated in the contribution to the net optomechanical coupling rate per photon  $g_0$  (see Fig. 7(f)), compared with MB effects. A significant value of net  $g_0$  of 32 kHz, was determined for the SBL by the interacting mechanical and orthogonally-polarized optical modes (see Supplementary Materials for details). Such large optomechanical coupling rate was coming from two relatively large photoelastic coefficients (i.e.,  $p_{55} =$

0.145 and  $p_{56} = -0.151$ ) and similar distributions of the interacting modes, favoring a considerably large overlap integrand of  $g_0$ . This value represents nearly a three-fold improvement compared with the state-of-the-art report (i.e.,  $g_0$  of 12.5 kHz from Ref. [17]). Detailed analysis can be found in Supplementary Materials.

The discrepancy of Brillouin shift,  $\sim 0.02$  GHz, between simulation and experiment was possibly caused by imperfection of fabrications and the anisotropy of the LNOI microresonator (such as photoelastic and stiffness tensors) that was not considered in the current analyses.

## **Further Discussion and Conclusion**

Our measured spectrum revealed only the Stokes Brillouin lasing process, with no observed anti-Stokes emission. This is attributed to the current inter-modal Brillouin scattering configuration, which does not simultaneously satisfy the phase-matching condition for anti-Stokes lasing. Consequently, the Stokes and anti-Stokes processes were effectively decoupled, resulting in efficient single-sideband Stokes gain with a 6.8% slope efficiency [33]. Future cavity design improvements, incorporating more than two sets of cavity modes into the nonlinear Brillouin interactions, could enable the simultaneous harnessing of both Stokes and anti-Stokes processes. While larger cavities offer higher Q-factors and potentially lower thresholds [12], the compactness and electro-optic tunability of the narrow-bandwidth coherent radiation demonstrated here are highly promising for scalable PICs. Furthermore, enhancing the Q-factor of our microcavity and minimizing transferred pump laser noise could achieve sub-hertz Stokes Brillouin laser linewidths in future implementations.

In conclusion, we have demonstrated a compact, narrow-linewidth, electro-optically tunable Brillouin laser utilizing a small LNOI microdisk resonator and a novel phase-matching scheme. This laser achieves a strong optomechanical coupling rate and a low threshold, alongside a 6.8% slope efficiency, all within a highly compact device. This development represents a significant advancement, paving the way for applications in coherent information processing, precision metrology, and high-density photonic integration.

## **Materials and Methods**

### **Experiments**

A tunable diode laser (Model TLB-6728, New Focus Inc.) was used as pump light source, and the pump light was controlled to be transverse-electrically (TE) polarized with an inline polarization controller (PC). And the light was amplified by an erbium-doped fiber amplifier (EDFA) and tuned by a variable optical attenuator (VOA). Then the input light was launched into a fiber circulator, and was coupled to the microdisk via a tapered fiber with a diameter of 2  $\mu\text{m}$ . The LNOI microdisk was mounted on a 6-axis nanopositioning motorized stage with spatial resolution of 5 nm. A real-time optical microscope imaging system which consists of an objective lens of numerical aperture of 0.25 and a charge coupled device (CCD) camera was mounted above the microdisk to monitor the coupled position. It is worth noting that the tapered fiber was placed in contact with the edge of the microdisk for introducing weak perturbation by carefully adjusting the coupled position. To improve the coupling stability, it is necessary to keep the tapered fiber tighten and fixed, which can be notably prevent mechanical vibration of the tapered fiber. The backward Brillouin scattering signal was also sent to the optical spectral analyzer (OSA, Model: AQ6370D, Yokogawa Inc.) through the circulator for spectral analysis with spectral resolution of 0.02 nm. Moreover, to more precise measure the wavelength interval between the pump wavelength and the Brillouin signal, the backward Brillouin scattering signal and the backward pump scattering signal were together sent to a high-speed photodetector (PD) connected with a real-time electrical spectral analyzer (ESA, Model: FSVA3030, Rohde & Schwarz Inc.) for generating beat note signal. Furthermore, to characterize the linewidths of the backward Brillouin laser signal, a tunable narrow bandpass filter with bandwidth of 0.8  $\mu\text{m}$  was used, enabling the separate the backward-scattering pump light. Here, a home-built optical delayed self-heterodyne interferometer using a single-mode fiber with a length of 5 km, was employed to measure the phase noise without deducting the effect caused by the limited optical delay, inevitably resulting in an underestimation of the intrinsic linewidth of the Brillouin laser. To precisely measure the intrinsic linewidth, a commercially available laser phase noise analyzer based on correlated self-heterodyne technique was also used to extract phase fluctuations of the laser signal for revealing Brillouin laser frequency noise, which has been eliminated the effect resulted from coherence of the limited delayed self-heterodyne narrow-linewidth signals.

## References

1. K. Kikuchi, Fundamentals of coherent optical fiber communications. *J. Lightwave Technol.* **34**, 157–179 (2016).
2. C. L. Degen, F. Reinhard, P. Cappellaro, Quantum sensing. *Rev. Mod. Phys.* **89**, 035002 (2017).
3. J. Kitching, S. Knappe, E. A. Donley, Atomic sensors – a review. *IEEE. Sens. J.* **11**, 1749–1758 (2011).
4. A. D. Ludlow, M. M. Boyd, J. Ye, E. Peik, P. O. Schmidt, Optical atomic clocks. *Rev. Mod. Phys.* **87**, 637–701 (2015).
5. S. Gundavarapu, G. M. Brodник, M. Puckett, T. Huffman, D. Bose, R. Behunin, J. Wu, T. Qiu, C. Pinho, N. Chauhan, J. Nohava, P. T. Rakich, K. D. Nelson, M. Salit, D. J. Blumenthal, Sub-hertz fundamental linewidth photonic integrated Brillouin laser. *Nat. Photonics* **13**, 60 (2019).
6. K. Y. Yang, D. Y. Oh, S. H. Lee, Q.-F. Yang, X. Yi, B. Shen, H. Wang, K. Vahala, Bridging ultrahigh-Q devices and photonic circuits. *Nat. Photonics* **12**, 297–302 (2018).
7. B. J. Eggleton, C. G. Poulton, P. T. Rakich, M. J. Steel, G. Bahl, Brillouin integrated photonics. *Nat. Photonics* **13**, 664–677 (2019).
8. M. Li, L. Chang, L. Wu, J. Staffa, J. Ling, U. A. Javid, S. Xue, Y. He, R. Lopez-Rios, T. J. Morin, H. Wang, B. Shen, S. Zeng, L. Zhu, K. J. Vahala, J. E. Bowers, Q. Lin, Integrated pockels laser. *Nat. Commun.* **13**, 5344 (2022).

9. J. Lin, S. Farajollahi, Z. Fang, N. Yao, R. Gao, J. Guan, L. Deng, T. Lu, M. Wang, H. Zhang, W. Fang, L. Qiao, Y. Cheng, *Adv. Photon.* **4**, 036001 (2022).
10. T. Lu, L. Yang, T. Carmon, B. Min, A narrow-linewidth on-chip toroid Raman laser. *IEEE J. Quantum Electron.* **47**, 320–326 (2011).
11. O. Florez, P. F. Jarschel, Y. A. Espinel, C. M. B. Cordeiro, T. P. Mayer Alegre, G. S. Wiederhecker, P. Dainese, Brillouin scattering self-cancellation. *Nat. Commun.* **7**, 11759 (2016).
12. I. S. Grudinin, A. B. Matsko, L. Maleki, Brillouin Lasing with a CaF<sub>2</sub> whispering gallery mode resonator. *Phys. Rev. Lett.* **102**, 043902 (2009).
13. S. Zhu, B. Xiao, B. Jiang, L. Shi, X. Zhang, Tunable Brillouin and Raman microlasers using hybrid microbottle resonators. *Nanophotonics* **8**, 931–940 (2019).
14. N. T. Otterstrom, R. O. Behunin, E. A. Kittlaus, Z. Wang, P. T. Rakich, A silicon Brillouin laser. *Science* **360**, 1113–1116 (2018).
15. Y. Bai, M. Zhang, Q. Shi, S. Ding, Y. Qin, Z. Xie, X. Jiang, M. Xiao, Brillouin-Kerr soliton frequency combs in an optical microresonator. *Phys. Rev. Lett.* **126**, 063901 (2021).
16. H. Zhang, T. Tan, H.-J. Chen, Y. Yu, W. Wang, B. Chang, Y. Liang, Y. Guo, H. Zhou, H. Xia Q. Gong, C. W. Wong, Y. Rao, Y.-F. Xiao, B. Yao, Soliton microcombs multiplexing using intracavity-stimulated Brillouin lasers. *Phys. Rev. Lett.* **130**, 153802 (2023).
17. M. Wang, Z.-G. Hu, C. Lao, Y. Wang, X. Jin, X. Zhou, Y. Lei, Z. Wang, W. Liu, Q.-F. Yang, B.-B. Li, Taming Brillouin optomechanics using supermode microresonators. *Phys. Rev. X* **14**, 011056 (2024).
18. Y. Li, D. Xia, H. Cheng, L. Luo, L. Wang, S. Zeng, S. Yang, L. Li, B. Chen, B. Zhang, Z. Li, Low-loss compact chalcogenide microresonators for efficient stimulated Brillouin lasers. *Opt. Lett.* **49**, 4529–4532 (2024).
19. Z. Xie, F. Bo, J. Lin, H. Hu, X. Cai, X. Tian, Z. Fang, J. Chen, M. Wang, F. Chen, Y. Cheng, J. Xu, S. Zhu, Recent development in integrated Lithium niobate photonics. *Adv. Phys. X* **9**, 2322739 (2024).
20. Y. Jia, L. Wang, F. Chen, Ion-cut lithium niobate on insulator technology: Recent advances and perspectives. *Appl. Phys. Rev.* **8**, 011307 (2021).
21. D. Zhu, L. Shao, M. Yu, R. Cheng, B. Desiatov, C. J. Xin, Y. Hu, J. Holzgrafe, S. Ghosh, A. Shams-Ansari, E. Puma, N. Sinclair, C. Reimer, M. Zhang, M. Lončar, Integrated photonics on thin-film lithium niobate. *Adv. Opt. Photon.* **13**, 242–352 (2021).
22. G. Chen, N. Li, J. D. Ng, H.-L. Lin, Y. Zhou, Y. H. Fu, L. Y. T. Lee, Y. Yu, A.-Q. Liu, A. J. Danner, Advances in lithium niobate photonics: development status and perspectives. *Adv. Photon.* **4**, 034003 (2022).
23. R. Wu, J. Zhang, N. Yao, W. Fang, L. Qiao, Z. Chai, J. Lin, Y. Cheng, Lithium niobate micro-disk resonators of quality factors above 10<sup>7</sup>. *Opt. Lett.* **43**, 4116–4118 (2018).
24. C. C. Rodrigues, R. O. Zurita, T. P. M. Alegre, G. S. Wiederhecker, Stimulated Brillouin scattering by surface acoustic waves in lithium niobate waveguides. *J. Opt. Soc. Am. B* **40**, D56–D63 (2023).
25. Y.-H. Yang, J.-Q. Wang, Z.-X. Zhu, X.-B. Xu, Q. Zhang, J. Lu, Y. Zeng, C.-H. Dong, L. Sun, G.-C. Guo, C.-L. Zou, Stimulated Brillouin interaction between guided phonons and photons in a lithium niobate waveguide. *Sci. China Phys. Mech. Astron.* **67**, 214221 (2024).
26. W. Wang, Y. Yu, Y. Li, Z. Bai, G. Wang, K. Li, C. Song, Z. Wang, S. Li, Y. Wang, Z. Lu, Y. Li, T. Liu, X. Yan, Tailorable Brillouin light scattering in a lithium niobate waveguide. *Appl. Sci.* **11**, 8390 (2021).
27. N. Chauhan, A. Isichenko, K. Liu, J. Wang, Q. Zhao, R. O. Behunin, P. T. Rakich, A. M. Jayich, C. Fertig, C. W. Hoyt, D. J. Blumenthal, Visible light photonic integrated Brillouin laser. *Nat. Commun.* **12**, 4685 (2021).
28. J. E. Toney. Lithium niobate photonics (Artech House, 2015).
29. D. Xu, F. Yang, D. Chen, F. Wei, H. Cai, Z. Fang, R. Qu, Laser phase and frequency noise measurement by Michelson interferometer composed of a 3×3 optical fiber coupler. *Opt. Express* **23**, 22386–22393 (2015).
30. Z. Yuan, H. Wang, L. Wu, M. Gao, K. Vahala, Linewidth enhancement factor in a microcavity Brillouin laser. *Optica* **7**, 1150–1153 (2020).

31. G. S. Wiederhecker, P. Dainese, T. P. Mayer Alegre, Brillouin optomechanics in nanophotonic structures. *APL Photonics* **4**, 071101 (2019).
32. J. Li, H. Lee, T. Chen, K. J. Vahala, Characterization of a high coherence, Brillouin microcavity laser on silicon. *Opt. Express* **20**, 20170–20180 (2012).
33. E. A. Kittlaus, N. T. Otterstrom, P. T. Rakich, On-chip inter-modal Brillouin scattering. *Nat. Commun.* **8**, 15819 (2017).

### **Acknowledgments**

We thank Peking university Yangtze delta institute of optoelectronics for providing the laser phase noise measurement system (iFN5000).